

# REGIONAL WAVEFIELD ANALYSIS USING THREE-COMPONENT SEISMIC ARRAY DATA

Gregory S. Wagner & Thomas J. Owens  
Department of Geological Sciences  
University of South Carolina  
Columbia, SC 29208

AFOSR Contract No. F49620 - 94 - 1 - 0066

## Abstract

An example of regional wavefield analysis using three-component seismic array data is presented. We examine the high-frequency (0.5–5.0 Hz) wavefields from three events that occurred in or near the Nevada Test Site (NTS), two underground nuclear tests and one earthquake, observed at the IRIS Joint Seismic Program three-component array located approximately 400 km to the south at Piñon Flat Observatory (PFO). The three-component array data are first displayed as broadband bearing-time records (BTR) which provide a time history of the propagation direction of coherent direct and scattered signals crossing the array; these displays are used primarily as a guide for further analysis. The BTRs reveal significant differences in the three wavefields. These differences are somewhat surprising in light of the fact that these data have essentially sampled the same terrain between NTS and PFO. The BTRs show that the  $P$  and  $S$  codas, and the  $L_g$  wavetrains for these three events contain a considerable amount of forward scattered/multipathed energy. It is only with the arrival of surface waves (apparent velocity approximately 3 km/s) that the coda becomes more random in nature. The fact that much of this later coda cannot be modeled as plane waves suggests that it is not scattered from distant sources.

The  $L_g$  wavetrain for one event is examined in detail. A spectrogram, and  $P$ - $SV$ ,  $SH$  BTRs computed using the three-component array data reveal that the early portion of this particular  $L_g$  wavetrain is comprised of two linearly polarized  $SH$ /Love waves and a Rayleigh wave. The most prominent arrival in this  $L_g$  wavetrain is examined in more detail. When plotted in three-dimensions, the tangential and elliptical components of particle motion are more pronounced. High-resolution frequency-wavenumber analysis reveals that this section of this particular  $L_g$  is comprised of simultaneously arriving  $PSV_z$  (principal-component in the  $P$ - $SV$  plane with predominantly vertical motion) and  $SH$ /Love modes with different frequencies, wavenumbers, and slightly different apparent velocities. The nearly identical radial and Hilbert-transformed vertical component waveform data provide further evidence that the  $P$ - $SV$  energy is a Rayleigh as opposed to a shallow incidence angle  $SV$  wave.

**key words:** array, polarization, seismic phase identification, regional wave propagation, scattering, multipathing, seismic coda.

- **Objective**

The objective of our research is to: (i) improve event detection, phase identification and parameter and waveform estimation, (ii) provide an improved understanding of regional wave propagation, and (iii) to aid in the characterization of lithospheric heterogeneities. These goals are addressed by combining analysis of observed three-component array data and numerical simulations of elastic wave propagation in realistic earth structures.

- **Preliminary Research Results**

For this report we examine three events that occurred in the Nevada Test Site area (NTS); two are underground nuclear tests and one an earthquake. These data were collected as part of the Incorporated Research Institutions for Seismology (IRIS) consortium's Joint Seismic Program at Piñon Flat, California (PFO) (Al-Shukri *et al.*, 1991). The upper part of Figure 1 shows the PFO array geometry and a regional seismicity map (from CALNET and CALTECH catalogs,  $M_L > 3$ ) for the three-month PFO experiment. The locations of NTS and PFO are shown on the seismicity map. The lower part of Figure 1 shows the broadband and 0.5–5.0 Hz bandpass filtered data for the three events examined for this report. These waveforms are event-wise normalized with amplitudes relative to the maximum in the broadband and bandpass filtered data, respectively, listed with each trace. Table 1 lists the origin times, locations, *etc.*, for the three events examined for this report.

- *Processing Approach*

The bandpass filtered (0.5–5.0 Hz) three-component array data are analyzed using the approach discussed in Wagner & Owens (1995b). Briefly, the magnitude of the multidimensional enhanced minimum-variance (EMV) spectrum is the inverse of the minimum eigenvalue,  $\lambda_3(\theta, \omega, c)$ , of the matrix

$$\mathbf{C}(\theta, \omega, c) = \mathbf{E}^\dagger(\theta, \omega, c) \mathbf{U}_N(\omega) \mathbf{\Lambda}_N(\omega) \mathbf{U}_N^\dagger(\omega) \mathbf{E}(\theta, \omega, c) \quad (1)$$

where  $^\dagger$  denotes conjugate transpose,  $\mathbf{U}_N(\omega)$  is the unitary matrix whose columns are the [eigen]vectors that span the signal subspace's (Owsley, 1978) orthogonal complement,  $\mathbf{\Lambda}_N(\omega)$  is the diagonal matrix containing the associated eigenvalues, and

$$\mathbf{E}(\theta, \omega, c) = \begin{bmatrix} \uparrow & \uparrow & \uparrow \\ \mathbf{e}_Z(\theta, \omega, c) & \mathbf{e}_{NS}(\theta, \omega, c) & \mathbf{e}_{EW}(\theta, \omega, c) \\ \downarrow & \downarrow & \downarrow \end{bmatrix} \quad (2)$$

where the  $\mathbf{e}_i(\theta, \omega, c)$  are mutually orthogonal steering vectors for Z,NS,EW polarized plane waves traveling in direction  $\theta$  with apparent velocity  $c$ . The eigenvector associated with the minimum eigenvalue,  $\mathbf{p}_3(\theta, \omega, c)$ , is in general complex and parameterizes the component-wise amplitude and phase relations. The mode vector for the  $\omega$  frequency component is

$$\mathbf{e}(\theta, \omega, c, \mathbf{p}_3) = \mathbf{E}(\theta, \omega, c) \mathbf{p}_3(\theta, \omega, c) \quad (3)$$

Note that Equation 3 merely provides high-resolution estimates of the mode vectors. Waveform estimates are obtained by projecting the  $\mathbf{e}(\theta, \omega, c, \mathbf{p}_3)$  onto the signal subspace (Gething, 1971)

$$\mathbf{w}(\theta, \omega, c, \mathbf{p}_3) = \mathbf{\Lambda}_S^{1/2}(\omega) \mathbf{e}^\dagger(\theta, \omega, c, \mathbf{p}_3) \mathbf{U}_S(\omega) \quad (4)$$

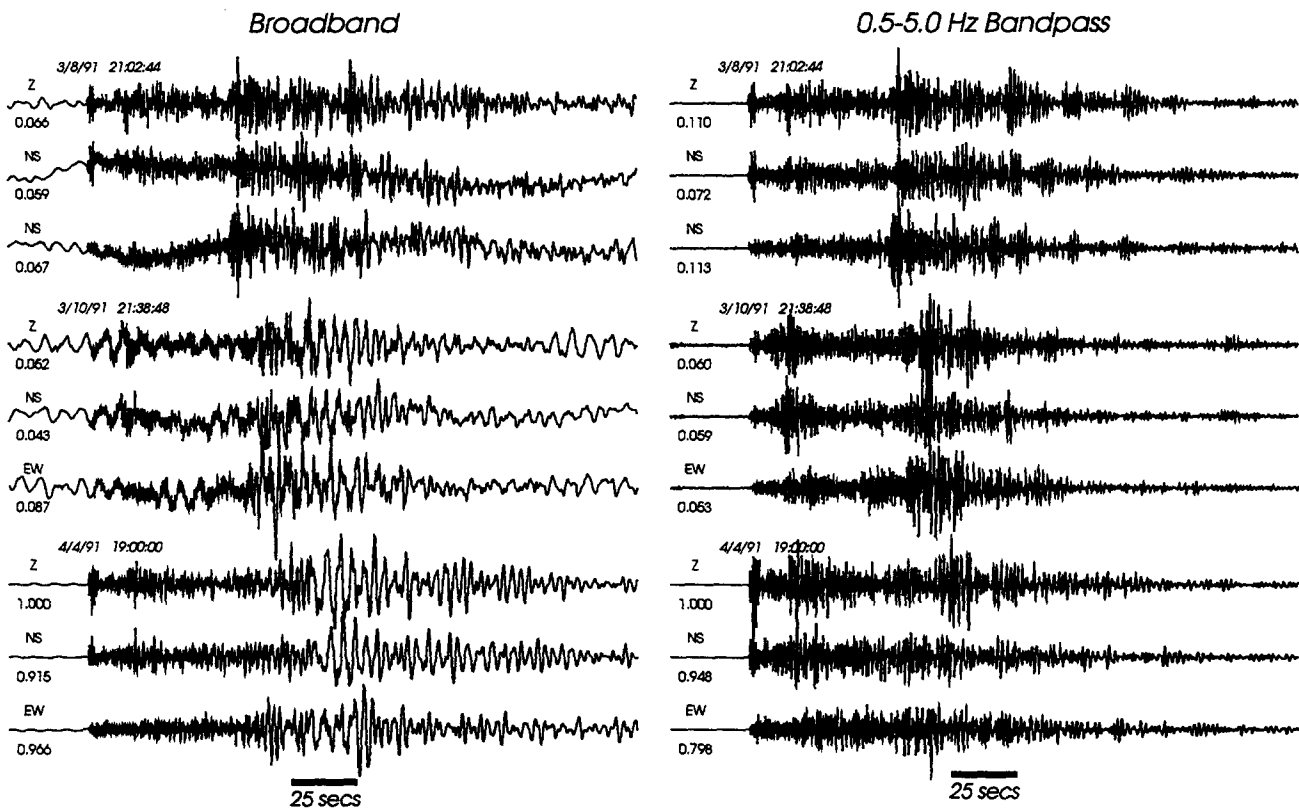
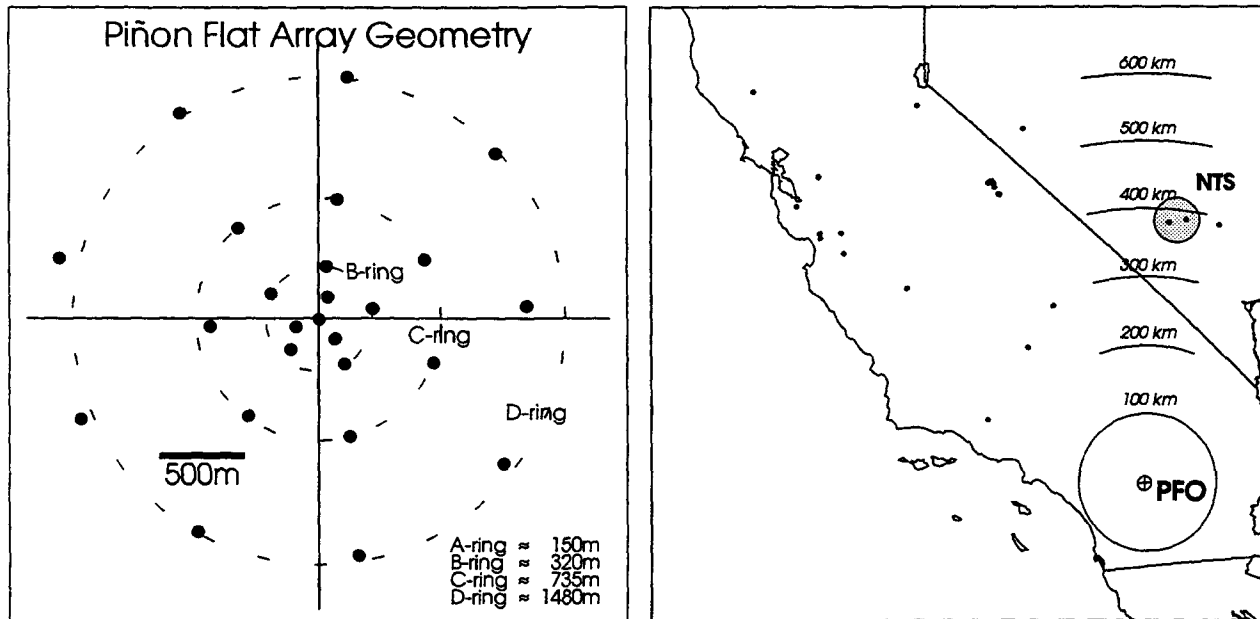


Figure 1: Top, the PFO array geometry and regional seismicity ( $M_L > 3$ ) that occurred during the three-month PFO experiment. Bottom, the broadband and 0.5–5.0 Hz bandpass filtered data for the three events examined for this report. The waveforms are event-wise normalized with amplitudes relative to the maximum in the broadband and bandpass filtered data, respectively, listed with each trace See Table 1 for origin times, locations, etc..

date	hr:mn:sec	lat° (N)	lon° (E)	z (m)	$M_L$	delta°	BAZ°
03/08/91	21:02:45.40	37.104	-116.074	475	4.6	3.49	5.04
03/10/91	21:38:47.51	37.110	-115.232	5,000	4.0	3.63	15.67
04/04/91	19:00:00.00	37.296	-116.313	629	5.4	3.67	3.01

Table 1: Origin times, latitudes, longitudes, depths (meters), magnitudes, distances, and back azimuths from PFO for the three events examined in this report.

where  $\mathbf{U}_S(\omega)$  is the unitary matrix whose columns are the [eigen]vectors that span the signal subspace, and  $\mathbf{\Lambda}_S^{1/2}(\omega)$  is the diagonal matrix containing the square roots of the associated eigenvalues. Knowing the direction of energy flux,  $\theta$ , the wavetype can be determined based on the particle motion parameterized by  $\mathbf{p}_3(\theta, \omega, c)$ . The associated power flux density is

$$\mathcal{P}(\theta, \omega, c, \mathbf{p}_3) = \mathbf{e}^\dagger(\theta, \omega, c, \mathbf{p}_3) \mathbf{U}_S(\omega) \mathbf{\Lambda}_S(\omega) \mathbf{U}_S^\dagger(\omega) \mathbf{e}(\theta, \omega, c, \mathbf{p}_3) . \quad (5)$$

The following section provides an outline of the analysis procedure using this approach.

- *Data Analysis*

Our analysis typically begins by computing broadband bearing-time records (BTR) of the three-component array data (Wagner & Owens, 1995a). BTRs provide a time history of the propagation direction of the coherent direct and scattered arrivals crossing the array. The BTRs serve primarily as a guide to further analysis. Figure 2 shows the broadband (0.5–5.0 Hz) EMV BTRs for the three events shown in Figure 1. Also calculated but not displayed in Figure 2 are the component-wise amplitude and phase relations for the coherent modes (i.e. the  $\mathbf{p}_3(\theta, \omega, c)$ ). It is this information, combined with the direction-of-arrival (DOA) information, that allows us to identify the wavetype. Apparent velocity information is, unfortunately, lost with this particular broadband implementation.

Figure 2 raises several questions of particular interest for regional monitoring. First, the increased interest in regional characterization is both motivated by and based on the assumption that events that occur in the same region and sample the same terrain will be similarly affected by the structure, and that this effect occurs independent of source magnitude. One might expect, therefore, that the wavefields for these three events would exhibit similar characteristic. This is, however, not the case. The second observation is that the  $P$  and  $S$  codas, and the  $L_g$  wavetrains contain considerable amounts of forward scattered/multipathed energy. It is only with the arrival of the surface wave energy (apparent velocity of approximately 3 km/s) that the coda begins to exhibit more varied/random DOAs. The fact that much of this later coda cannot be modeled as plane waves suggests that it is not the product of scattering from distant sources.

Of the three events examined for this report, the event that occurred on 3/8/91 has the best developed  $L_g$  wavetrain. Because  $L_g$  is of considerable interest in CTBT monitoring and regional wave propagation in general, we conducted detailed analysis of the  $L_g$  wavetrain for this event. Figure 3 shows the spectrogram (Equation 5 as a function of time) for the 4–3 km/s apparent velocity window. The Z,NS,EW data are plotted with the spectrogram to help provide insight into the way each of the components contributes to the total field (note that these data are essentially naturally rotated). Similar plots showing the relative magnitudes of the Z,R,T components of  $\mathbf{p}_3(\theta, \omega, c)$  as red, blue, green can be used to help identify wavetypes. Figure 3 shows the higher frequency  $L_g$  wavetrain proceeding and superimposed on the lower frequency  $S$ -coda and surface wave energy. The early  $L_g$  (11–16 secs in Figure 3) is comprised of three distinct phases with two simultaneous

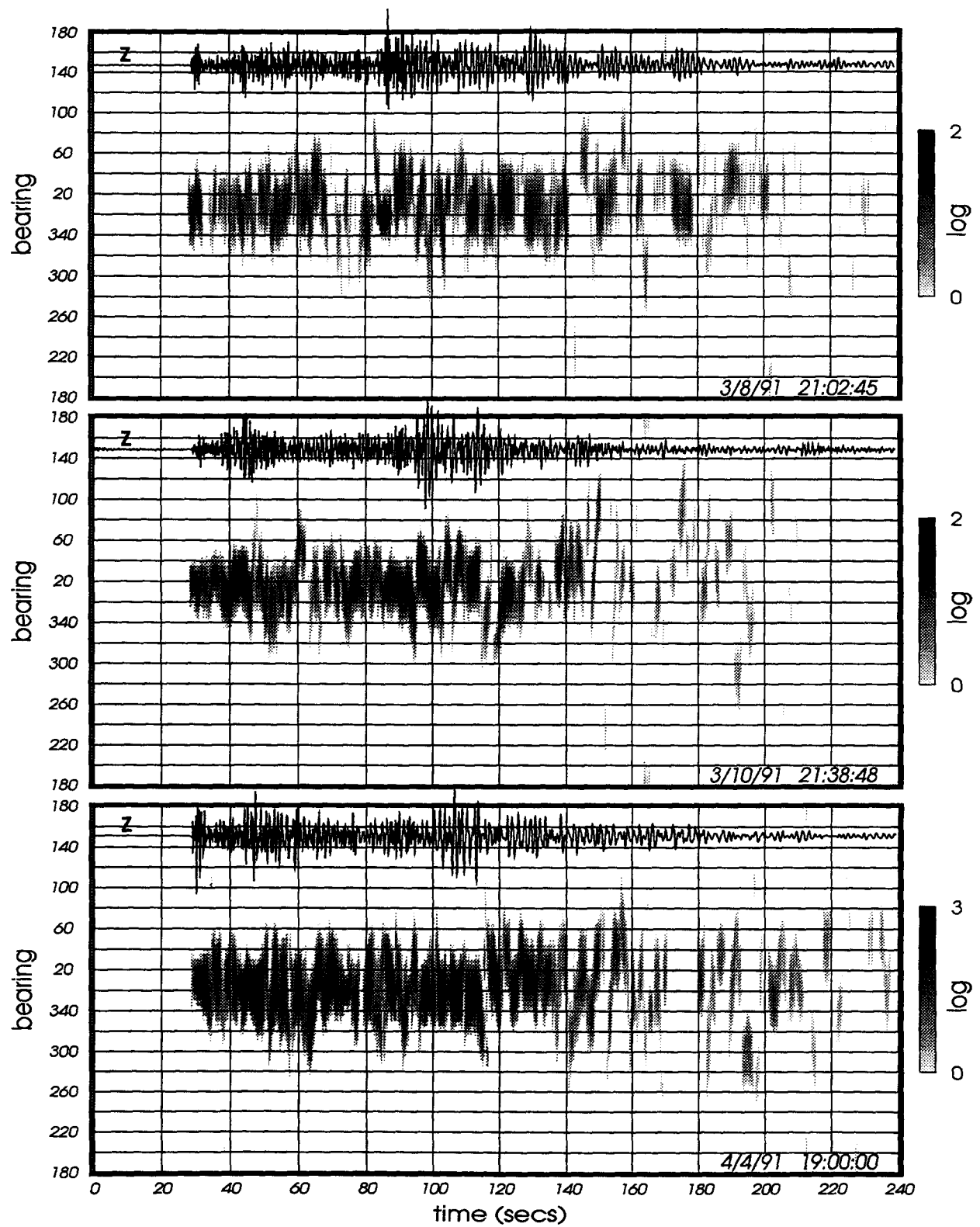


Figure 2: Three-component, broadband (0.5–5.0 Hz) bearing-time records for the three events listed in Table 1.

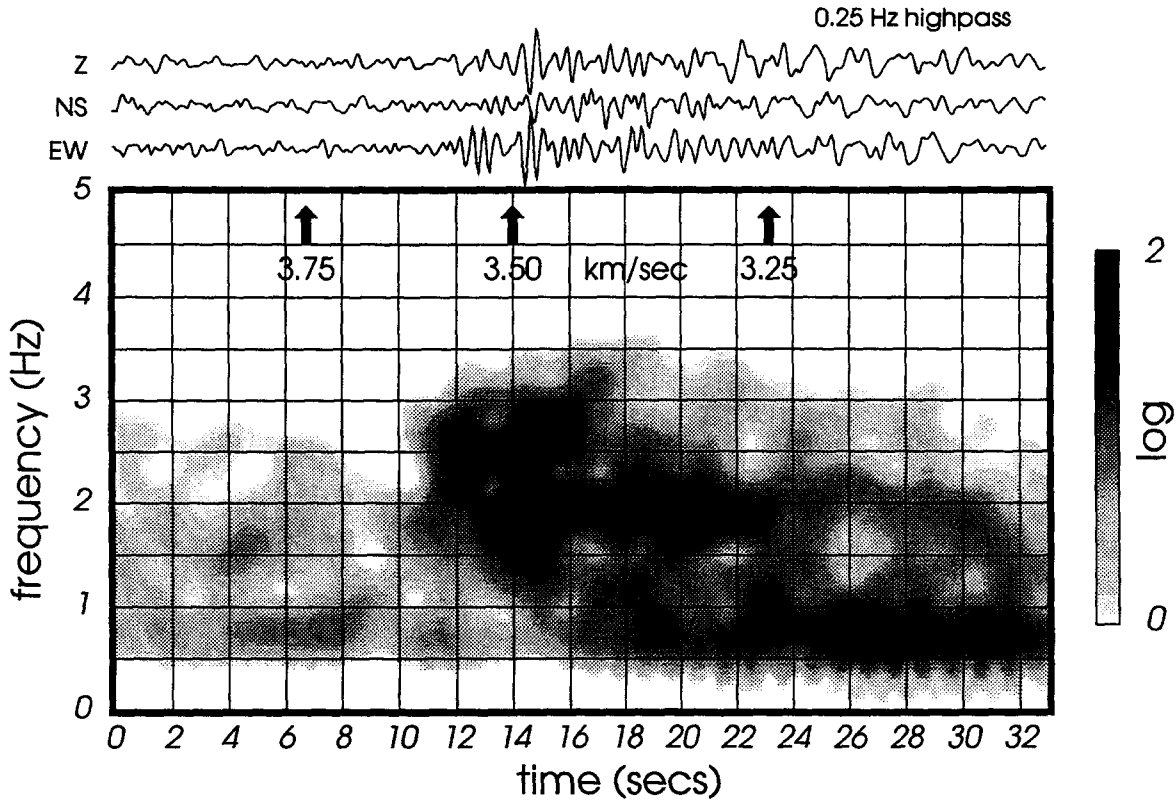


Figure 3: Spectrogram for the 4–3 km/s apparent velocity window for event 3/8/91.

arrivals at approximately 14.5 secs. Based on  $\mathbf{p}_3(\theta, \omega, c)$ , these two phases are identified as linearly polarized Love/*SH* and Rayleigh waves with peak frequencies of approximately 2.5 and 1.8 Hz, respectively. Figure 4 shows the BTRs for the total field, and the field decomposed into *P-SV* and *SH* components (Wagner & Owens, 1993). These *P-SV*, *SH* component BTRs reveal the characteristic simultaneously-arriving mixed-mode nature of *L<sub>g</sub>*.

Further analysis was conducted on the most prominent arrival in the *L<sub>g</sub>* wavetrain for this event (3/8/91). The top part of Figure 5 (part A) shows the three-dimensional particle motion for the 1 sec window containing the largest arrival in the *L<sub>g</sub>* wavetrain. When viewed from the NNW and ENE, the tangential and elliptical components of particle motion are more pronounced. The middle part of Figure 5 (part B) shows the EMV frequency-wavenumber ( $\omega$ -*k*) spectra for the *PSV<sub>z</sub>*, *PSV<sub>r</sub>* and *SH* components (Wagner & Owens, 1993). The  $\omega$ -*k* spectra were computed (using the complex analytic signal) for the beam steered in the direction indicated by the BTRs. The  $\omega$ -*k* analysis reveals that this data window contains simultaneously arriving *PSV<sub>z</sub>* (principal-component in *P-SV* plane with predominantly vertical motion) and *SH*/Love modes with different frequencies, wavenumbers, and slightly different apparent velocities. The bottom part of Figure 5 (part C) shows the vertical- and radial-component waveforms (left), and the radial- and Hilbert-transformed ( $\mathcal{H}$ ) vertical-component waveforms (right). The elliptical particle motion (part A) and the nearly identical  $\mathcal{H}(Z)$  and  $\mathcal{H}(R)$  waveforms concur with the component-wise phase relations parameterized by  $\mathbf{p}_3(\theta, \omega, c)$ , all of which suggest that the arrival isolated on the *PSV<sub>z</sub>* spectrum is a Rayleigh as opposed to a shallow incidence angle *SV* wave.

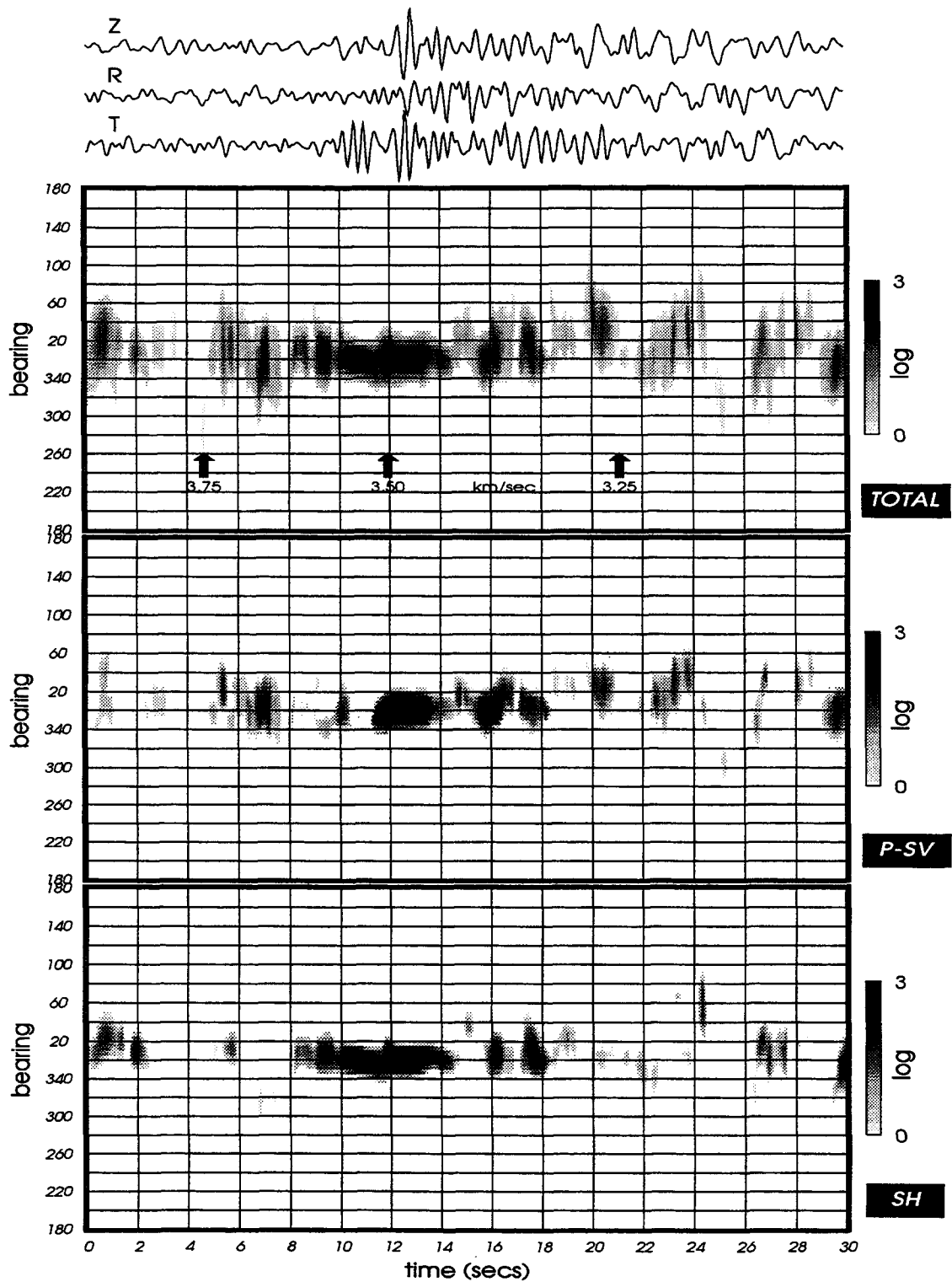


Figure 4: Total field, *P-SV*, and *SH* bearing-time records for the 0.5–5.0 Hz passband, 4–3 km/s apparent velocity window for the event that occurred on 3/8/91 (see Table 1 for origin times, location, etc.).

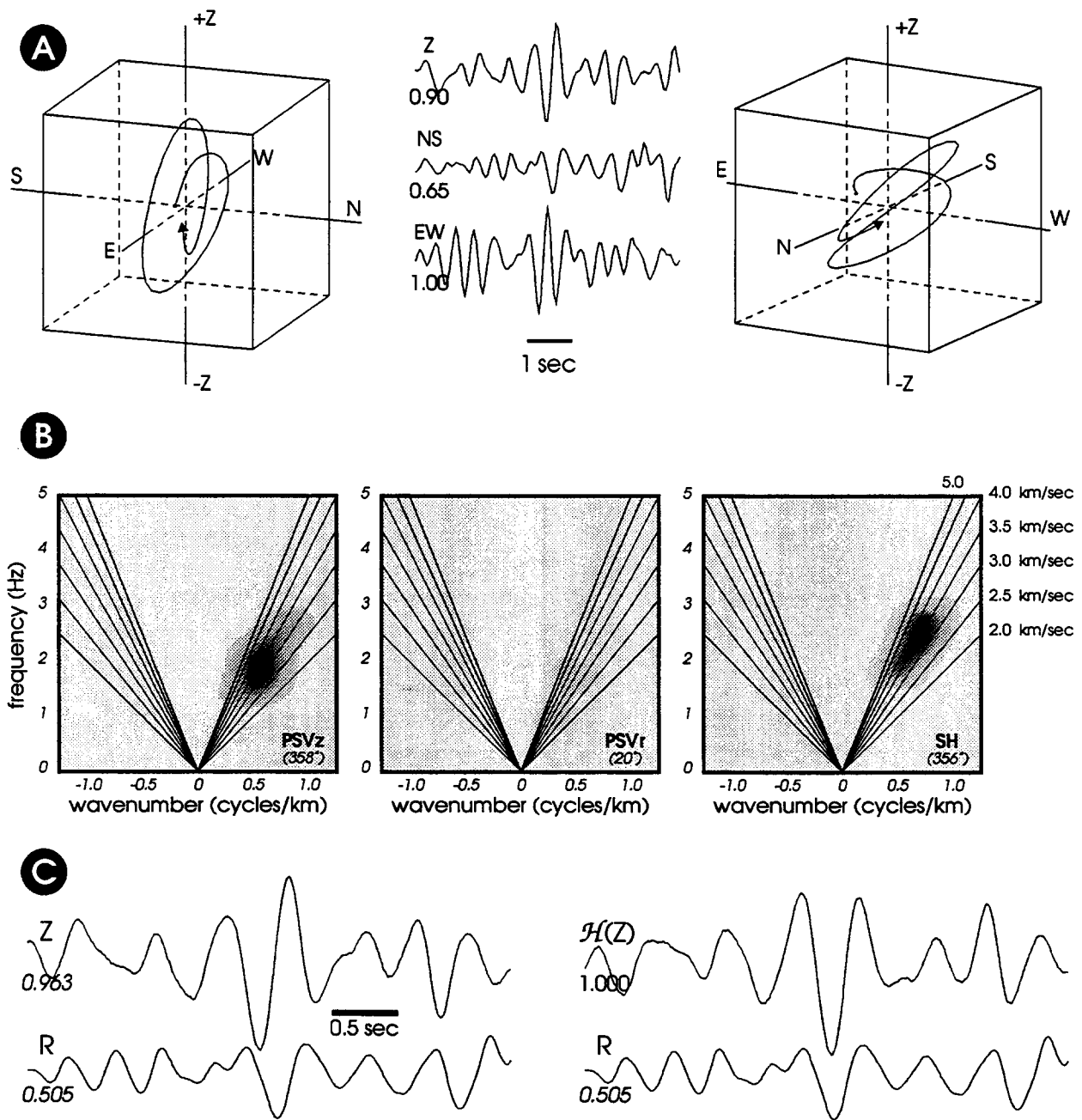


Figure 5: Top (A), three-dimensional particle motion, viewed from the ENE (left) and NNW (right), for the 1 sec window containing the most prominent arrival in the  $L_g$  wavetrain for event 3/8/91. Middle (B),  $PSV_z$ ,  $PSV_r$ ,  $SH$  frequency-wavenumber spectra for the most prominent  $L_g$  arrival; the three spectra are plotted using the same amplitude scale. Bottom (C), the vertical- and radial-component waveforms, and the radial- and Hilbert-transformed vertical-component waveforms of the early  $L_g$ .

## • Conclusions, Recommendations & Future Plans

This report provides an example of analysis of the regional wavefield using three-component seismic array data. Our analysis of  $L_g$  provides an example of the wealth of information provided by the elastic wavefield and three-component array data. Vertical-component array data provide no information about the  $SH$ /Love component of the seismic wavefield, and reduce our ability to detect, identify, and obtain truly representative waveform estimate for  $P$ ,  $SV$  and Rayleigh waves. Elastic wavefield decomposition using single-site three-component data requires additional information (i.e. wavetype, propagation direction) that may not be available in a realistic monitoring situation. Three-component array data do not restrict our analysis to the vertically polarized component of the wavefield, and allow us to resolve the numerous problems and ambiguities inherent in elastic wavefield decomposition using data from isolated three-component sensors.

The complex problems we are faced with in monitoring a CTBT are exacerbated by not taking full advantage of the wealth of information provided by the elastic wavefield. Elastic waveform data provide the best and sometimes our only source of information about source processes and earth structure. Regional waveform data play a vital role in CTBT monitoring by providing information about smaller events that may not be observed at teleseismic distances. Broadband three-component array data provide a multidimensional, spatially and temporally unaliased sampling of the regional wavefield that permits a nearly comprehensive decomposition of the elastic wavefield. These data allow us to address and answer fundamental questions about seismic wave propagation that simply cannot be answered conclusively using data from vertical-component arrays or networks of isolated single- and/or three-component sensors. The availability of broadband three-component array data collected in regions around the globe would provide a unique and invaluable resource to the entire community.

Future plans are to continue analysis of these data to provide an improved understanding of regional wave propagation, to improve event detection, phase identification and waveform estimation, and to aid in the characterization of lithospheric heterogeneities. Our analysis is limited somewhat by the availability of three-component array data from different regions. Without data from other regions it is not possible to ascertain which of the characteristics observed in PFO data are unique to this region in particular, and which are true for regional wave propagation in general.

## References

- Al-Shukri, H., Owens, T., Pavlis, G., Roecker, S., Vernon, F., and Wagner, G., 1991. Data report for the 1991 Piñon Flat broadband array experiment *IRIS/PASSCAL Data Report*, pp. 27.
- Gething, P. J. D., 1971. Analysis of multicomponent wavefields, *Proc. IEE*, **118**(10), 1333–1338.
- Owsley, N. L., 1978. Adaptive data orthogonalization, *Proc. IEEE Int. Conf. Acoust., Speech, Signal Processing*, 109–112.
- Wagner, G. S. and Owens, T. J., 1993. Broadband bearing-time records of three-component seismic array data and their application to the study of local earthquake coda, *Geophys. Res. Letters*, **20**(17), 1823–1826.
- Wagner, G. S. and Owens, T. J., 1995a. Broadband eigen-analysis for three-component seismic array data, *IEEE Trans. on Signal Processing*, **43**(7), 1738–1741.
- Wagner, G. S. and Owens, T. J., 1995b. A processing approach for three-component seismic array data, submitted to *Geophysical Journal International*, January, 1995.